Control and Stability Analysis of Current-Controlled Grid-Connected Inverters in Asymmetrical Grids

Ali Akhavan, *Senior Member, IEEE*, Saeed Golestan, *Senior Member, IEEE*, Juan C. Vasquez, *Senior Member, IEEE*, and Josep M. Guerrero, *Fellow, IEEE*

***Abstract*—In symmetrical grids, single-input single-output (SISO) analysis/design tools are applicable for the analysis and design of grid-tied inverter systems as their average $\alpha\beta$- or *dq*-frame models are to a high extent decoupled (in the high-frequency range). In this way, designing the control system could be done in a straightforward manner. However, this is not the case under asymmetrical grids. In this condition, the interaction between different phases makes the average model of the grid-tied inverter a multi-input multioutput (MIMO) system, and therefore, complicated to analyze and design. To cope with this challenge, this article deals with deriving the MIMO control system considering the impact of the asymmetrical grid. Then, the MIMO system turns into two decoupled SISO systems. Thus, a simple yet accurate model is developed which intuitively demonstrates the effect of the grid asymmetry on creating coupling between current control loops. In this way, the stability analysis could be carried out irrespective of the MIMO system difficulties. The experimental results validate the accuracy of the proposed approach in asymmetrical grid conditions.**

***Index Terms*—Asymmetrical grids, grid-connected inverters, interaction, multi-input multioutput (MIMO) system, stability.**

I. Introduction

GRID-CONNECTED inverters, which often use an *LCL* output filter, are one of the most important elements in renewable-energy-based systems [1]. The resonance of the *LCL* filter, especially in weak grids with a varying grid impedance, is among the most important factors that jeopardize the stability of the system [2]. To address this issue, various passive and active resonance damping methods have been proposed in the literature [3]–[9]. Another challenge, especially in active damping methods, is the negative effect of the pulsewidth modulation (PWM)/measurement delay on the resonance damping [2]. To overcome this issue, a large number of approaches have been reported which are mostly based on introducing a positive phase to the control system using various kinds of high- or band-pass filters [10]–[12]. Also, many research works have focused on developing the control system for enhancing the system stability and robustness, by considering both resonance and delay issues [13]–[18].

A common feature of almost all the conventional methods is assuming a symmetrical grid condition. In this situation, the three-phase inverter and its control system are modeled as a single-input single-output (SISO) control loop, and classical control approaches are applied for the analysis/design [19]. This approach is simple and quite accurate under symmetrical grid conditions. However, it may not be practical under asymmetrical ac grids.

In distributed power grids many factors such as asymmetrical power line impedance and asymmetrical/single-phase local loads make the equivalent grid impedance seen by the inverter asymmetric. In such a condition, there is a coupling effect among different parts of the system and therefore, the system should be modeled by a multi-input multioutput (MIMO) system with cross-coupling terms between the α- and β-axes. It makes the system more complex from design and stability analysis points of view. Neglecting the cross-coupling terms for simplifying the control system may result in poor control system design and imprecise stability analysis, which in turn may jeopardize the stability of the system in real applications. Hence, a powerful tool for stability analysis of the system in asymmetrical grids is immediately demanded. This is an area of great potential that could attract attention.

Some recent investigations have proved that asymmetrical grid line impedance has an adverse effect on the stability of grid-connected inverters [20], [21]. The stability of an *L*-filtered grid-connected inverter in the asymmetrical grid using the harmonic linearization method is investigated in [20]. However, the extension of this method to an inverter with the *LCL* filter complicates the model derivation. In [22], a system consisting of an inverter with an *L* filter is modeled in the asymmetrical grid line impedance using decoupled matrices and then, the generalized Nyquist criterion (GNC) is applied to predict the stability of the system. It is noted that the control system of an *LCL*-filtered inverter has more internal loops than an *L*-filtered inverter including resonance damping and capacitor voltage loops, which in turn bring more complexity to the system. Wu *et al.* [21] proposed an approach based on the individual channel method [23] to model a three-phase inverter with the *LCL* filter in asymmetrical grids, where a passive damping method is used to mitigate the resonance of the *LCL* filter. In this method, transfer functions of cross-coupled terms between

Manuscript received 6 November 2021; revised 7 February 2022, 6 April 2022, and 2 June 2022; accepted 13 July 2022. Date of publication 18 July 2022; date of current version 6 September 2022. This work was supported by VILLUM FONDEN under the VILLUM Investigator under Grant 25920, Center for Research on Microgrids. Recommended for publication by Associate Editor K. Sun. *(Corresponding author: Ali Akhavan.)*

The authors are with the AAU Energy, Aalborg University, 9220 Aalborg, Denmark (e-mail: alak@energy.aau.dk; sgd@energy.aau.dk; juq@energy.aau.dk; joz@energy.aau.dk).

Color versions of one or more figures in this article are available at https://doi.org/10.1109/TPEL.2022.3191839.

Digital Object Identifier 10.1109/TPEL.2022.3191839

the α- and β-axes in the MIMO system are derived to simplify the control system. However, using active damping methods is preferred to passive ones to avoid power losses. In this situation, the number of cross-coupled terms will increase, which may increase the system complexity and may demand additional tasks for model derivation, consequently. In [24], the MIMO system is decomposed into three SISO closed-loop subsystems in the *dq* frame, and the classical SISO Nyquist stability criterion is applied for the stability investigation. To this end, the effects of the dc-bus-voltage control and phase-locked loop (PLL) have been considered. Then, the derived MIMO system that includes all these controllers' effects is turned into three SISO systems. Even though admirable, however, the effect of grid impedance asymmetry has not been addressed. Suh *et al.* [25] proposed a control scheme that improves the transient response of an ac/dc converter in an unbalanced condition. To this end, the control scheme employs individual current regulators in the *dq* synchronous frame in each positive and negative sequence. However, analyzing both positive and negative sequences in a unified control system increases the system complexity considerably. On the other hand, designing such a complex control system needs to be addressed appropriately. The stability of the system under asymmetrical local loads was investigated in [26], where conservative power theory (CPT) is employed for the active compensation of the imbalance local load current and eliminating the effect of the local load by adding an offset to the inverter reference current. Nevertheless, the effect of asymmetrical grid line impedance on the system stability is not addressed. In [27], a mathematical model for positive and negative frames of a grid-connected inverter is proposed, which is based on the multifrequency proportional-resonant controller in the $\alpha\beta$ frame. Afterward, a new concept for instantaneous active and reactive powers is introduced in unbalanced conditions. The linear time-periodic (LTP) method is another approach that has recently attracted attention for modeling systems that suffer from unbalanced conditions, especially in the low-frequency range [28]. However, designing the control system, especially for the MIMO systems, is not mature enough. On the other hand, the stability analysis methods that are used for this modeling method are not straightforward [29]. Zhang *et al.* [30] proposed an approach that is based on the harmonic-transfer-function (HTF) for asymmetrical grids, where the sequence impedances are modeled in the HTF framework and the effect of the PLL is considered on the internal loops, elaborately. However, the order of the system should be reduced based on the property of frequency couplings since the HTFs are of infinite dimension and cannot be directly analyzed. In [31], the dynamics of a system consisting of an *LCL* filter are represented using the complex-based method, in which the root locus analysis is employed for designing the control system for unbalanced power networks. A multifrequency admittance based on the complex-valued model is proposed in [32] to characterize the frequency-coupling dynamics of inverters in unbalanced grid voltage conditions. In [33], a multifrequency admittance matrix has been used for the stability analysis of a single-phase inverter, in which the frequency coupling effect caused by the PLL is investigated. Using the harmonic-state-space approach [34] is another method for harmonic modeling and stability analysis, however, the model derivation is not easy because of the large model dimensions. In [35], the stability of microgrid clusters in the asymmetrical grid is investigated by lumping the frequency-domain model of all inverters, and then, applying the GNC.

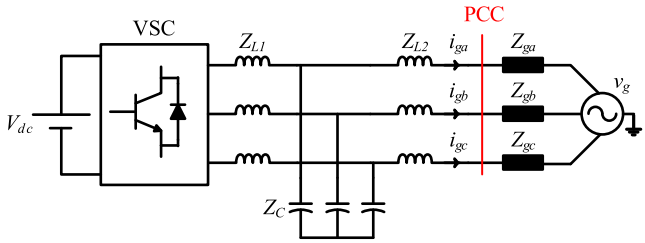

Fig. 1. Topology of a three-phase grid-connected inverter.

To analyze the system in a simple yet precise way, this article presents a method for the stability analysis of inverters in asymmetrical grids. In this method, the MIMO model of a grid-tied inverter equipped with an active damping method is first derived intuitively. Then, the MIMO model is decomposed into two SISO systems by considering the effect of the cross-coupling terms. In this way, the stability analysis could be done using classical SISO methods, without neglecting any dynamics, which in turn guarantees the accuracy of the proposed method. Note that the proposed modeling is valid for both cases of asymmetrical grid line impedance and asymmetrical local loads.

The rest of this article is summarized as follows. Section II explains the system description and control method, and then discusses the effect of asymmetrical grids. Section III is devoted to the MIMO model derivation and its transformation into two SISO systems for a simple stability investigation. The stability analysis of the derived model is investigated in Section IV. The validity of the proposed approach is verified using the experimental results in Section V, for the case of the asymmetrical grid line impedance and local load. Finally, Section VI concludes this article.

II. System Description and Problem Definition

This section first provides a system overview and then explains the negative aspects of asymmetrical grids on the converter stability.

A. System Description

Fig. 1 depicts the structure of a three-phase grid-connected inverter, where Z_{L1}, Z_{L2}, and Z_C, as shown in (1), are the impedances of the inverter-side inductor, grid-side inductor, and filter capacitor, respectively

$$Z_{L1} = L_1\, s, \quad Z_{L2} = L_2\, s, \quad Z_C = \frac{1}{Cs}. \tag{1}$$

Also, Z_g (Z_{ga}, Z_{gb}, and Z_{gc}) is the grid impedance, which is defined in a general form here because it could be symmetrical or asymmetrical.

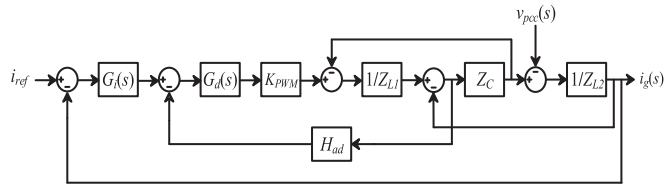

Fig. 2. Control block diagram of a current-controlled grid-connected inverter.

The well-known control block diagram of a current-controlled grid-connected inverter that uses a capacitor current feedback for the active damping is shown in Fig. 2 [2], [10], [12]. In this figure, $G_i(s)$ and H_{ad} are the grid-side current controller and proportional controller of the active damping loop, respectively, and i_g is the injected current to the grid. Also, $v_{\rm pcc}$ is the point of common coupling (PCC) voltage that is shown in Fig. 1. The transfer function of the inverter is modeled by $K_{\rm PWM} = V_{\rm dc}/(2V_{\rm tri})$, where $V_{\rm dc}$ and $V_{\rm tri}$ are the dc voltage and amplitude of the triangular carrier, respectively [2]. $G_d(s)$ models the aggregated computational and PWM delays that is expressed as follows [2], [36]:

$$G_d(s) = e^{-1.5\,T_s s} \tag{2}$$

where T_s is the sampling period. Also, it should be pointed out that the bandwidth of the PLL is designed intentionally much lower than the internal loops so that its effect on the control system could be neglected, without considerably affecting the accuracy of the modeling [14]. This allows us to keep the system as simple as possible.

From Fig. 2, the loop gain of the control system could be derived as follows:

$$T(s) = \frac{K_{\rm PWM} G_i(s) G_d(s)}{s^3 L_1 L_2 C + s^2 L_2 C H_{ad} K_{\rm PWM} G_d(s) + s(L_1 + L_2)}. \tag{3}$$

As could be found in Figs. 2 and (3), the impact of grid impedance is overlooked in the dynamics of the control system, while it could affect the stability of the whole system [12], [19]. Therefore, designing the control system and stability analysis should be done considering the effect of grid impedance. Otherwise, it may jeopardize the stability of the system. The situation could be even worse when the inverter is connected to an asymmetrical grid with different values of grid impedance or local load per phase. In the next section, the adverse effect of asymmetricity in grids will be clarified.

B. Effect of Asymmetrical Grids

From Fig. 1, the mathematical relation between PCC voltage and injected current to the grid could be derived in the *abc* frame as follows:

$$\begin{bmatrix} v_{pcc,a} \\ v_{pcc,b} \\ v_{pcc,c} \end{bmatrix} - \begin{bmatrix} v_{g,a} \\ v_{g,b} \\ v_{g,c} \end{bmatrix} = \begin{bmatrix} Z_{ga} & 0 & 0 \\ 0 & Z_{gb} & 0 \\ 0 & 0 & Z_{gc} \end{bmatrix} \begin{bmatrix} i_{ga} \\ i_{gb} \\ i_{gc} \end{bmatrix} \tag{4}$$

where $v_{pcc,i}$ and $v_{g,i}$ are the phase PCC voltage and grid voltage for phase i ($i = a, b, c$), respectively. By using the Clarke transform, the above equation turns to

$$\begin{bmatrix} v_{pcc,\alpha} \\ v_{pcc,\beta} \end{bmatrix} - \begin{bmatrix} v_{g,\alpha} \\ v_{g,\beta} \end{bmatrix} = \boldsymbol{T}_{abc\to\alpha\beta} \times \begin{bmatrix} Z_{ga} & 0 & 0 \\ 0 & Z_{gb} & 0 \\ 0 & 0 & Z_{gc} \end{bmatrix} \times \boldsymbol{T}_{\alpha\beta\to abc} \times \begin{bmatrix} i_{g,\alpha} \\ i_{g,\beta} \end{bmatrix} \tag{5}$$

where $v_{pcc,\alpha}$, $v_{pcc,\beta}$, $v_{g,\alpha}$, $v_{g,\beta}$ and also, $i_{g,\alpha}$ and $i_{g,\beta}$ are the PCC voltage, grid voltage, and injected current to the grid in the α- and β-axes, respectively. Also, $\boldsymbol{T}_{abc\to\alpha\beta}$ and $\boldsymbol{T}_{\alpha\beta\to abc}$ are matrices for transforming from *abc* to $\alpha\beta$ frame and vice versa, respectively, as presented in (6). The gain 2/3 is considered for $\boldsymbol{T}_{abc\to\alpha\beta}$ in (6) to preserve the amplitude of waveforms constant after the transformation

$$\boldsymbol{T}_{abc\to\alpha\beta} = \frac{2}{3}\begin{bmatrix} 1 & -\frac{1}{2} & -\frac{1}{2} \\ 0 & \frac{\sqrt{3}}{2} & -\frac{\sqrt{3}}{2} \end{bmatrix}, \boldsymbol{T}_{\alpha\beta\to abc} = \begin{bmatrix} 1 & -\frac{1}{2} & -\frac{1}{2} \\ 0 & \frac{\sqrt{3}}{2} & -\frac{\sqrt{3}}{2} \end{bmatrix}^T. \tag{6}$$

It should be noted that a three-phase three-wire system is considered in this article; therefore, there is no zero-sequence component in (6). By substituting (6) into (5), this equation can be represented as follows:

$$\begin{bmatrix} v_{pcc,\alpha} \\ v_{pcc,\beta} \end{bmatrix} - \begin{bmatrix} v_{g,\alpha} \\ v_{g,\beta} \end{bmatrix} = \begin{bmatrix} Z_{g,\alpha\alpha} & Z_{g,\alpha\beta} \\ Z_{g,\beta\alpha} & Z_{g,\beta\beta} \end{bmatrix} \begin{bmatrix} i_{g,\alpha} \\ i_{g,\beta} \end{bmatrix} \tag{7}$$

where

$$\begin{aligned} Z_{g,\alpha\alpha} &= \tfrac{2}{3} Z_{ga} + \tfrac{1}{6} Z_{gb} + \tfrac{1}{6} Z_{gc} \\ Z_{g,\alpha\beta} &= Z_{g,\beta\alpha} = \tfrac{\sqrt{3}}{6}(Z_{gc} - Z_{gb}) \\ Z_{g,\beta\beta} &= \tfrac{1}{2} Z_{gb} + \tfrac{1}{2} Z_{gc}. \end{aligned} \tag{8}$$

From (7) and (8), it could be immediately found that, in asymmetrical grids, α- and β- components of the grid-injected current are coupled together through nondiagonal terms of the impedance matrix in (7). Some stability issues may be caused if the grid impedance effect is neglected. According to (8), even though in the case of $Z_{gb} = Z_{gc}$, the nondiagonal terms are equal to zero ($Z_{g,\alpha\beta} = Z_{g,\beta\alpha} = 0$), yet $Z_{g,\alpha\alpha} \neq Z_{g,\beta\beta}$, which reveals that the inverter may see a different grid impedance at its output in the α- and β-axes. In this case, designing a similar control system for both α- and β-axes may jeopardize the stability of the system. The next section discusses the modeling of this asymmetricity for the stability analysis.

III. Modeling the System in Asymmetrical Grids

In the previous section, it was found that there is a coupling between α and β components of the grid-injected current in asymmetrical grids. Therefore, the control system should be modeled as an MIMO system to consider this coupling for the sake of stability analysis.

A. MIMO Model Derivation

From the findings in the previous section and keeping (7) in mind, the traditional control block diagram of the inverter in Fig. 2 turns into a two-input two-output system as depicted in Fig. 3, where the cross-coupling terms between α- and β-axes show the system complexity raised by the grid asymmetricity.

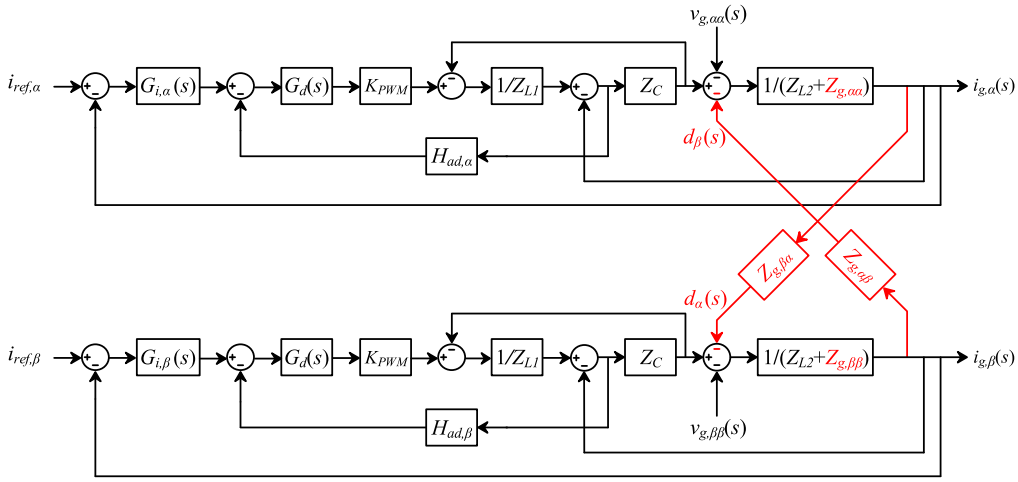

Fig. 3. MIMO control block diagram of a grid-connected inverter in an asymmetrical grid.

Note that the current and active damping controllers in Fig. 3 are named with α and β subscript in different axes, to point out that the control system could be different on each axis.

Various control methods have been proposed for MIMO systems [37]–[39]. However, most of them need extensive mathematical derivation, which in turn makes the control system design and stability analysis complicated. On the other hand, the accuracy of some of these methods is a matter of concern in highly coupled MIMO systems [40].

Perhaps, the simplest possible way to reduce the analysis complexity of MIMO systems is by neglecting their cross-coupling terms. In this way, only the effect of diagonal impedance terms in (7) will be considered. Even though simple, however, it may lead to an imprecise stability evaluation. Therefore, an intuitive method for simple yet accurate system analysis is demanded, without neglecting the system dynamics.

B. Decomposing the MIMO System Into Two SISO Subsystems

By decomposing the derived MIMO system into separate SISO subsystems, well-established SISO methods instead of complex MIMO ones can be used for investigating the system behavior under different conditions [40], [41]. To this end, the transfer function from $d_\beta(s)$ to $i_{g,\alpha}(s)$, and also, the transfer function from $d_\alpha(s)$ to $i_{g,\beta}(s)$, should be derived, first. It is worthy to note that d_α and d_β are defined as disturbance inputs caused by α- and β-axes, respectively. According to Fig. 3 and applying the block diagram algebra, the aforementioned transfer functions could be derived as (9) and (10) shown at the bottom of this page. In this way, the 2×2 MIMO control system could be turned into two decoupled SISO subsystems in the α- and β-axes, as Fig. 4 shows, considering the cross-coupling terms between axes. Hence, the system could be evaluated simply, in asymmetrical grids without loss of dynamics, which is one of the advantages of the proposed method in this article.

The dashed boxes in Fig. 4 show the main difference between the control system in asymmetrical grids with the traditional one that is shown in Fig. 2, where an additional feedback path (it is shown in red) is introduced in each axis because of the asymmetricity of the grid. It is noted that in a symmetrical grid, the cross-coupling terms are zero, and only the grid impedance could be inserted instead of $Z_{g,\alpha\alpha}$ and $Z_{g,\beta\beta}$ for considering the effect of grid impedance in the control system design [13]. To reveal the effect of cross-coupling terms, the Bode plots of the feedback path in the dashed boxes are depicted in Fig. 5 using the system parameters in Table I, for both α- and β-axes. The transfer function associated with these Bode plots are presented as follows:

$$G_{CC,\alpha}(s) = Z_{g,\beta\alpha}(s)\Delta_{\alpha\beta}(s)Z_{g,\alpha\beta}(s) \tag{11}$$

$$G_{CC,\beta}(s) = Z_{g,\alpha\beta}(s)\Delta_{\beta\alpha}(s)Z_{g,\beta\alpha}(s). \tag{12}$$

As shown in Fig. 5, the coupling magnitude is magnified for both axes as frequency increases. This magnification, if neglected, may cause harmonic instability. Fig. 5 reveals that unlike a symmetrical grid, where the cross-coupling terms are zero, the asymmetrical grid possesses a highly coupled system, especially at high frequencies.

$$\Delta_{\alpha\beta}(s) = \left.\frac{i_{g,\beta}}{d_\alpha}\right|_{i_{ref,\beta}=0} = \frac{Z_{L1}(s)+Z_C(s)+G_d(s)K_{\mathrm{PWM}}H_{ad,\beta}}{Z_{L1}(s)(Z_{L2}(s)+Z_{g,\beta\beta}(s))+Z_{L1}(s)Z_C(s)+Z_C(s)(Z_{L2}(s)+Z_{g,\beta\beta}(s))+G_d(s)K_{\mathrm{PWM}}H_{ad,\beta}(Z_{L2}(s)+Z_{g,\beta\beta}(s))+G_{i,\beta}(s)G_d(s)K_{PWM}Z_C(s)} \tag{9}$$

$$\Delta_{\beta\alpha}(s) = \left.\frac{i_{g,\alpha}}{d_\beta}\right|_{i_{ref,\alpha}=0} = \frac{Z_{L1}(s)+Z_C(s)+G_d(s)K_{\mathrm{PWM}}H_{ad,\alpha}}{Z_{L1}(s)(Z_{L2}(s)+Z_{g,\alpha\alpha}(s))+Z_{L1}(s)Z_C(s)+Z_C(s)(Z_{L2}(s)+Z_{g,\alpha\alpha}(s))+G_d(s)K_{\mathrm{PWM}}H_{ad,\alpha}(Z_{L2}(s)+Z_{g,\alpha\alpha}(s))+G_{i,\alpha}(s)G_d(s)K_{\mathrm{PWM}}Z_C(s)}. \tag{10}$$

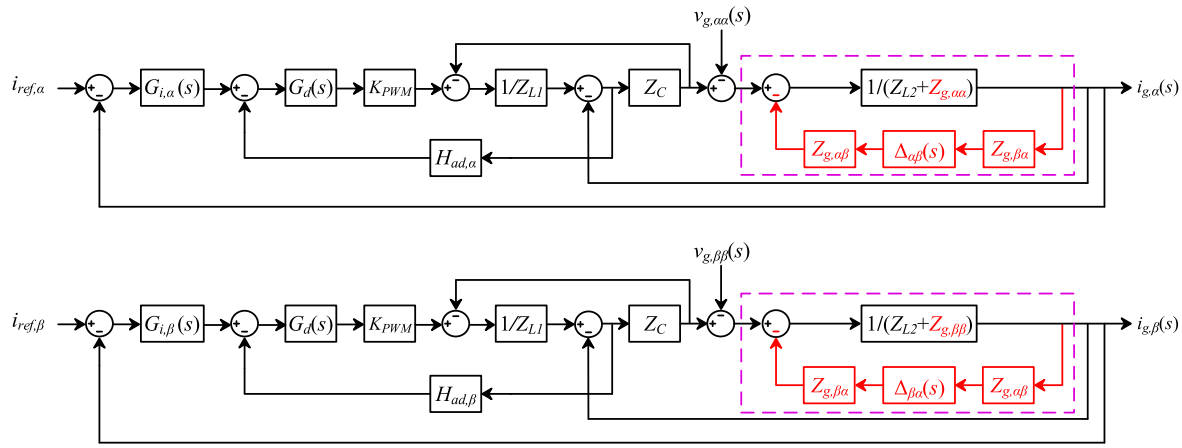

Fig. 4. Decoupled SISO subsystems derived from the MIMO control system.

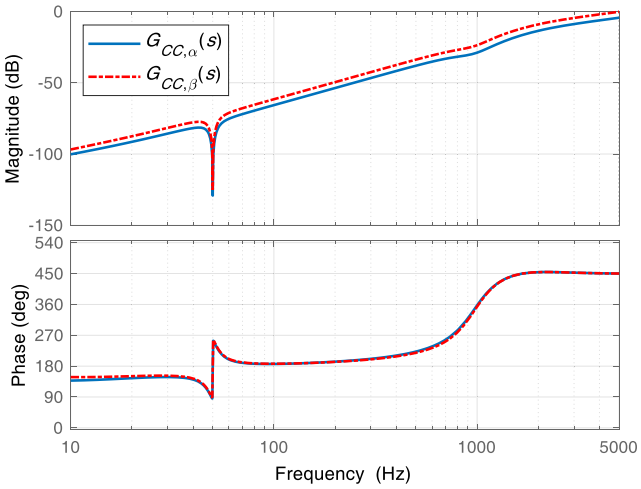

Fig. 5. Bode plots of the $G_{CC,\alpha}(s)$ and $G_{CC,\beta}(s)$.

TABLE I
SYSTEM AND CONTROL PARAMETERS

DC-link voltage, V_{dc}	650 V
Inverter-side inductor, L_1	1.8 mH
Filter capacitor, C	27 μF
Grid-side inductor, L_2	0.9 mH
Sampling frequency, f_s	10 kHz
Rated power of the inverter	2.2 kVA
Grid voltage, V_g	400 V (Line to line)
Grid frequency	50 Hz
Grid inductance, L_g	L_{ga} = 1 mH L_{gb} = 4 mH L_{gc} = 3 mH
Current controller (Proportional-resonant controller)	$G_{i,\alpha}(s) = G_{i,\beta}(s)$ $= k_p + k_r \times s / (s^2 + \omega_o^2)$ k_p = 13, k_r = 500
Active damping controller	$H_{ad,\alpha} = H_{ad,\beta} = 5$

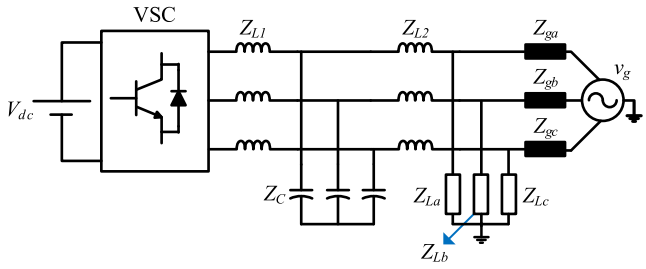

Fig. 6. Topology of a grid-connected system in the presence of a local load.

C. Effect of Local Loads

Fig. 6 illustrates the topology of a grid-connected system in the presence of a local load. In this figure, Z_L (Z_{La}, Z_{Lb}, and Z_{Lc}) is a typical local load connected to the three-phase system, which could be symmetrical or asymmetrical. Since the local load may affect the stability of the control system, its influence is investigated here. According to Fig. 4, the grid voltages in the α- and β-axes, which are $v_{g,\alpha\alpha}(s)$ and $v_{g,\beta\beta}(s)$, respectively, could be regarded as disturbance inputs and therefore, do not affect the stability of the system. Supposing $v_g = 0$ in Fig. 6, the local load in each phase could be regarded as a parallel connection with the grid impedance in its corresponding phase. Therefore, the impedance matrix in (4) in the *abc* frame could be turned into (13) in the presence of the local load

$$\boldsymbol{Z_{gl}}(s) = \begin{bmatrix} Z_{ga} \| Z_{La} & 0 & 0 \\ 0 & Z_{gb} \| Z_{Lb} & 0 \\ 0 & 0 & Z_{gc} \| Z_{Lc} \end{bmatrix}. \quad (13)$$

In (13), $\boldsymbol{Z_{gl}}(s)$ is the equivalent matrix that considers both the grid and local load impedances, and the symbol "$\|$" denotes the parallel connection of two impedances. In this way, the new impedance matrix could be transformed to the $\alpha\beta$ frame using (6), and the system modeling could be done following the guidelines in Sections III-A and III-B. Different scenarios such as the connection of a load between two phases could be considered, where the nondiagonal elements of the matrix $\boldsymbol{Z_{gl}}(s)$

will not be zero, anymore. However, because of the similarity of the modeling, it is not repeated here.

IV. Control System Design and Stability Analysis

In this part, the system stability is investigated under different case studies. The loop gain of the control systems in the α and β axes could be derived using Fig. 4, as presented at the bottom of this page. Note that these transfer functions have a general form that could be used for the case of asymmetricity in grid line impedance, local loads, or both.

A. Control System Design

Using (14) and (15), the system stability can be easily investigated. It is, however, not the case if designing the control parameters is intended, because all the control variables in the α-axis exist in the transfer function of the loop gain of the β-axis, and vice versa. It implies that both these transfer functions need to be considered simultaneously for designing the control parameters, which can be a challenging task

In order not to deal with this difficulty, one way is to design the control parameters of one axis (for instance, the α-axis), based on the passivity-based stability [12], [13], [18], and using the conventional control block diagram in Fig. 2. The main reason behind this idea is to simplify the design procedure. Passivity theory offers some guidelines for designing the control system so that the inverter has a passive behavior at all (or at least a wide range of) frequencies [42]. In this situation, it could be argued that the inverter is to a high extent robust, and could work stably in different conditions such as grid impedance variations [12]. In other words, even though the system asymmetry has not been considered in designing the α-axis, the system has high robustness against grid impedance variations thanks to the passivity approach. As the only difference between Fig. 2 and the α-axis of Fig. 4 is the grid impedance part (dashed box in Fig. 4) and based on the aforementioned explanation about passivity theory, the passivity of the control system in Fig. 2 can guarantee the passivity of the α-axis to a high extent. This approach gives proper base control parameters for simplifying the design procedure. Afterward, the control parameters of another axis (here, β-axis) could be designed based on the block diagram of Fig. 4, and by considering the coupling effect of the α-axis (taking parameters of the α axis into consideration). In this way, the control system could be designed for asymmetrical grids so that the coupling effect between axes is considered, and, the system stability could be investigated accurately.

According to the above explanations, the control parameters for the α-axis could be designed by following the passivity-theory-based guidelines in [12] and [13]. More details could be found in those references, and the control design procedure is not repeated here to save space. The control parameters for the α-axis could be summarized as: $k_{p,\alpha} = 13$, $k_{r,\alpha} = 500$, $H_{ad,\alpha} = 5$, where $k_{p,\alpha}$ and $k_{r,\alpha}$ are the proportional and resonant coefficients of the current controller in the α-axis ($G_{i,\alpha}(s)$), respectively. Also, $H_{ad,\alpha}$ is the active damping controller.

After designing the controller parameters of the α-axis, the controller parameters of the β-axis could be tuned according to Fig. 4 and (15) to consider the asymmetricity of the grid and/or local load. To this end, the active damping controller ($H_{ad,\beta}$) could be designed first. $H_{ad,\beta}$ could be optimized following the well-established method in [13] as follows:

$$0 < H_{ad,\beta} < \frac{\omega_r L_1 (2\cos(\omega_r T_s) - 1)}{K_{\text{PWM}} \sin(\omega_r T_s)} \tag{16}$$

where ω_r and T_s are the resonant angular frequency and sampling period, respectively. It is noted that the active damping controller should be designed to mitigate the resonance of the *LCL* filter by creating a virtual resistance in parallel with the filter capacitor. In this way, the grid asymmetry does not considerably affect its damping performance. Therefore, the proposed method in [13] still can be used for designing this controller.

The effect of the resonant term of the current controller could be neglected at frequencies much higher than the fundamental frequency [11], and it could be designed solely to provide a high control gain for tracking the fundamental component with a negligible steady-state error. Hence, supposing $G_{i,\beta}(s) \approx k_{p,\beta}$ at high frequencies, $T_\beta(s)$ could be rewritten as $T_\beta(s) = k_{p,\beta} \times G_{\text{plant},\beta}(s)$, where $G_{\text{plant},\beta}$ is presented in (17) shown at the bottom of this page. Then, the phase margin (PM) and gain margin (GM) of the $T_\beta(s)$ could be considered for designing the proportional term of the current controller ($k_{p,\beta}$) as follows:

$$\text{PM} = 180^\circ + \angle(k_{p,\beta} \times G_{\text{plant},\beta}(j\omega))\big|_{f_c} \tag{18}$$

$$\text{GM} = -20\log\left|k_{p,\beta} \times G_{\text{plant},\beta}(j\omega)\right|_{f_{180^\circ}} \tag{19}$$

where f_c and f_{180° are, respectively, the crossover frequency and the frequency in which the phase diagram crosses –180°.

From (18) and (19), it can be found that $k_{p,\beta}$ could be achieved based on the desired PM (k_{p,β_PM}) or GM (k_{p,β_GM}). A better

$$T_\alpha(s) = \frac{G_{i,\alpha}(s)G_d(s)Z_C(s)K_{\text{PWM}}}{Z_{L1}(s)Z_C(s) + (Z_{L2}(s) + Z_{g,\alpha\alpha}(s) + Z_{g,\alpha\beta}(s)\Delta_{\alpha\beta}(s)Z_{g,\beta\alpha}(s))(Z_{L1}(s) + Z_C(s) + K_{\text{PWM}}H_{ad,\alpha}G_d(s))} \tag{14}$$

$$T_\beta(s) = \frac{G_{i,\beta}(s)G_d(s)Z_C(s)K_{\text{PWM}}}{Z_{L1}(s)Z_C(s) + (Z_{L2}(s) + Z_{g,\beta\beta}(s) + Z_{g,\alpha\beta}(s)\Delta_{\beta\alpha}(s)Z_{g,\beta\alpha}(s))(Z_{L1}(s) + Z_C(s) + K_{\text{PWM}}H_{ad,\beta}G_d(s))}. \tag{15}$$

$$G_{\text{plant},\beta}(s) = \frac{G_d(s)Z_C(s)K_{\text{PWM}}}{Z_{L1}(s)Z_C(s) + (Z_{L2}(s) + Z_{g,\beta\beta}(s) + Z_{g,\alpha\beta}(s)\Delta_{\beta\alpha}(s)Z_{g,\beta\alpha}(s))(Z_{L1}(s) + Z_C(s) + K_{\text{PWM}}H_{ad,\beta}G_d(s))} \tag{17}$$

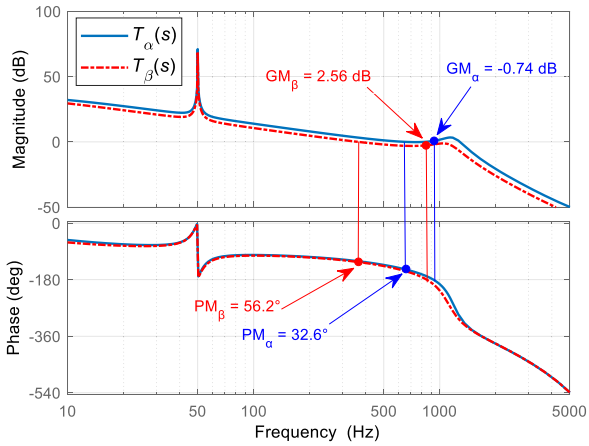

Fig. 7. Bode plots of the $T_\alpha(s)$ and $T_\beta(s)$ with $k_{p,\alpha} = k_{p,\beta} = 13$ (Case I) in an asymmetrical grid line impedance condition.

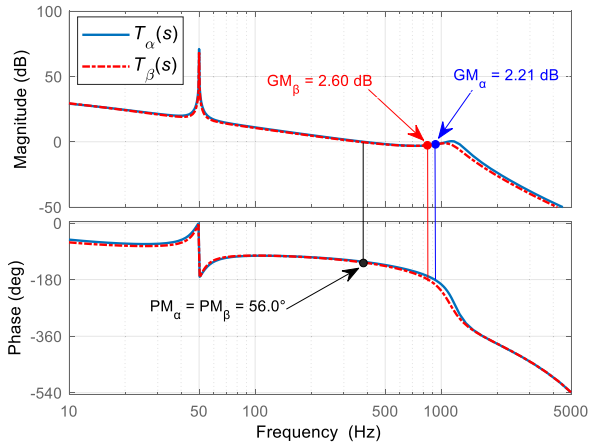

Fig. 8. Bode plots of the $T_\alpha(s)$ and $T_\beta(s)$ with $k_{p,\alpha} = 10$ and $k_{p,\beta} = 13$ (Case II) in an asymmetrical grid line impedance condition.

TABLE II
PROPORTIONAL GAIN OF CURRENT CONTROLLER IN AN ASYMMETRICAL GRID LINE IMPEDANCE CONDITION

Proportional gains of the current controller in α and β axes	$k_{p,\alpha}$	$k_{p,\beta}$
Case I (unstable)	13	13
Case II (stable)	10	13

way is to consider $k_{p,\beta}$ as $k_{p,\beta} = \min(k_{p,\beta\_\mathrm{PM}}, k_{p,\beta\_\mathrm{GM}})$ to satisfy the desired PM and GM at the same time. In this way, the control system could be accurately designed without complicated design methods for MIMO systems.

B. Asymmetricity in Grid Line Impedance

The Bode plots of the α and β loop gains for a grid-connected inverter with parameters presented in Table I are illustrated in Fig. 7, where the control parameters of both axes are intentionally selected identical to show the consequence of ignoring the coupling between axes. Note that in this case there is no local load. As shown in Fig. 7, the α-axis, despite having the same control parameters as the β one, is unstable because of having a negative GM. This problem, which makes the entire system unstable, is due to neglecting the coupling between axes.

The control parameters of the α- and β-axes could be redesigned using the proposed method so that two subsystems have almost equal PM and GM in an asymmetrical grid condition. By following the guidelines in Section IV-A, and changing the proportional gain of the current controller of the α-axis to 10, the new Bode plots of the α and β loop gains are presented in Fig. 8. As could be observed in this figure, both subsystems have almost similar PM and GM, and more importantly, both subsystems are stable unlike the previous case in Fig. 7. The proportional gains of the current controller for the former case (unstable case) and the latter one (stable case) for both α- and β-axes are summarized in Table II. Other parameters are the same as those presented in Table I.

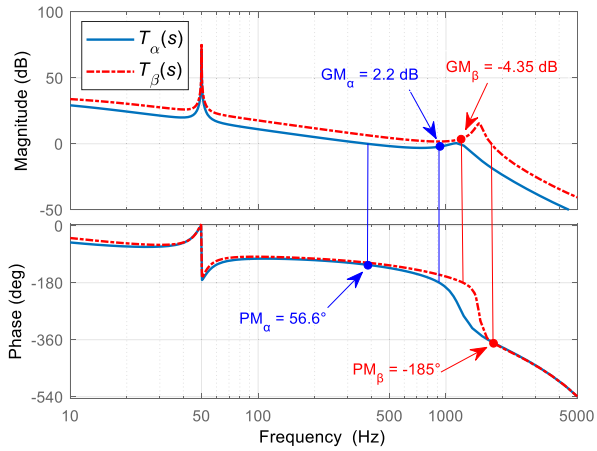

Fig. 9. Bode plots of the $T_\alpha(s)$ and $T_\beta(s)$ with $k_{p,\alpha} = 10$ and $k_{p,\beta} = 13$ (Case II) in an asymmetrical grid line impedance condition without considering the coupling terms.

Neglecting coupling terms in Fig. 3 will remove the feedback paths highlighted in red in Fig. 4. Therefore, the model of the system turns into the model of a grid-tied inverter under a balanced grid condition except that, instead of identical grid impedance for both axes, $Z_{\mathrm{g},\alpha\alpha}$ and $Z_{g,\beta\beta}$ are considered for the α- and β-axes, respectively. However, neglecting $Z_{\mathrm{g},\alpha\beta}$ and $Z_{\mathrm{g},\beta\alpha}$, and consequently, coupling terms in Fig. 3, may result in inaccurate stability predictions. In this part, the stability analysis is done without considering the coupling terms in Fig. 3. In this condition, the loop gain of the control systems for the α- and β-axes could be obtained as (20) and (21) shown at the bottom of the next page.

To show the consequence of ignoring the coupling terms, Case II in Table II is considered. According to Fig. 8, which is derived based on the accurate model presented in this article, the system should be stable. The Bode plots of $T_\alpha(s)$ and $T_\beta(s)$ are depicted in Fig. 9. As shown in this figure and unlike Fig. 8, the Bode plots indicate that the system is unstable because the PM and GM are negative on the β-axis. However, this is not a true prediction because the system has not been considered accurately and the

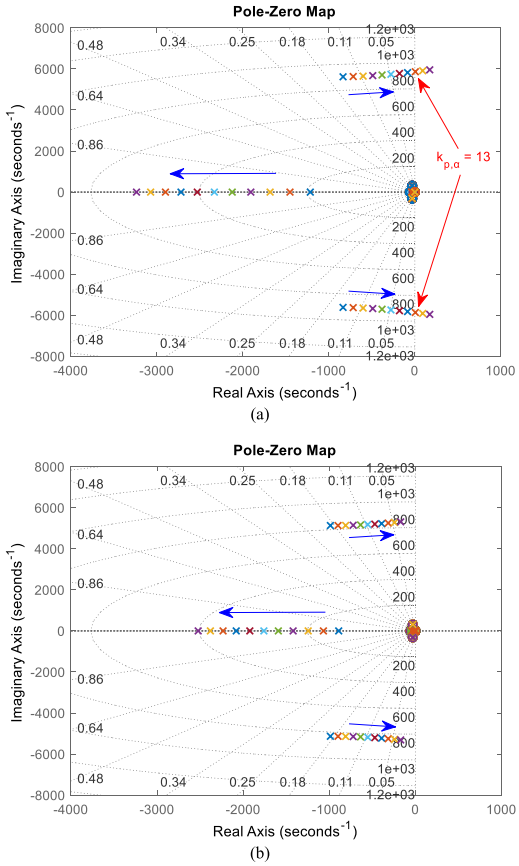

Fig. 10. Pole-zero maps of the system with changing $k_{p,\alpha}$ and $k_{p,\beta}$. (a) α-axis. (b) β-axis.

TABLE III
SYSTEM AND CONTROL PARAMETERS IN AN ASYMMETRICAL LOCAL LOAD CONDITION

Grid inductance, L_g	$L_{ga} = L_{gb} = L_{gc} = 3$ mH
Parallel *RC* local load	$R_a = 230\ \Omega$, $C_a = 13.5\ \mu$F $R_b = 115\ \Omega$, $C_b = 27\ \mu$F $R_c = 115\ \Omega$, $C_c = 13.5\ \mu$F
Control parameters in Case I (unstable)	$k_{p,\alpha} = k_{p,\beta} = 13$ $H_{ad,\alpha} = H_{ad,\beta} = 5$
Control parameters in Case II (stable)	$k_{p,\alpha} = k_{p,\beta} = 10$ $H_{ad,\alpha} = 6$, $H_{ad,\beta} = 7$

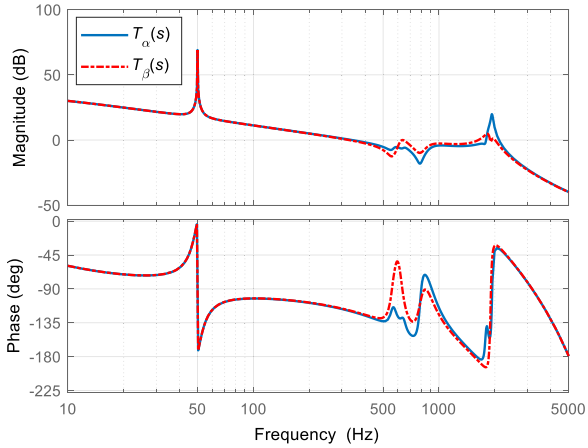

Fig. 11. Bode plots of the $T_\alpha(s)$ and $T_\beta(s)$ with $k_{p,\alpha} = k_{p,\beta} = 13$ and $H_{ad,\alpha} = H_{ad,\beta} = 5$ (Case I) in an asymmetrical *RC* local load condition.

analytical results of Fig. 8 are more accurate, where the coupling terms have been taken into account. The experimental result in the next section shows that contrary to the analytical results derived from Fig. 9, the system is stable and validates the stability analysis based on Fig. 8.

The loci of poles and zeros of the system with variation of two main parameters, i.e., the proportional gains of the current controller in α- and β-axes ($k_{p,\alpha}$ and $k_{p,\beta}$), are presented as shown in Fig. 10. To this end, $k_{p,\alpha}$ and $k_{p,\beta}$ are swept from 5 to 15 at the step of 1 to show the system dynamic behavior in the case of grid impedance asymmetry. Fig. 10(a) shows the pole-zero maps of the system in the α-axis while $k_{p,\alpha}$ is varied. As could be found, the system has a pole pair in the right half-plane when $k_{p,\alpha} = 13$. Similarly, the pole-zero maps of the system in the β-axis are shown in Fig. 10(b) when $k_{p,\beta}$ is swept. As could be observed in this figure, the system is stable for all values of $k_{p,\beta}$. The analysis presented in this section is compatible with the conclusion drawn from Fig. 7, where the Bode diagram of the system in the α-axis is unstable with $k_{p,\alpha} = 13$, yet the Bode diagram of the system in the β-axis is stable.

C. Asymmetricity in Local Load

The stability of a grid-connected inverter in the presence of an asymmetrical parallel *RC* local load is investigated in this section. The new system and control parameters for this case are summarized in Table III, while other ones are kept the same as before. The diagonal and cross-coupled terms of the equivalent grid impedance (consisting of the grid impedance and local load) seen by the inverter could be derived using (8) and (13).

The Bode diagrams of the α and β loop gains ($T_\alpha(s)$ and $T_\beta(s)$) with $k_{p,\alpha} = k_{p,\beta} = 13$ and $H_{ad,\alpha} = H_{ad,\beta} = 5$ (Case I in Table III) are plotted in Fig. 11. As could be observed, the stability investigation of the control system is quite difficult using the Bode plot, therefore, the Nyquist plot is used instead in this case.

$$T_\alpha(s) = \frac{G_{i,\alpha}(s)G_d(s)Z_C(s)K_{\text{PWM}}}{Z_{L1}(s)Z_C(s) + (Z_{L2}(s) + Z_{g,\alpha\alpha}(s))(Z_{L1}(s) + Z_C(s) + K_{\text{PWM}}H_{ad,\alpha}G_d(s))} \tag{20}$$

$$T_\beta(s) = \frac{G_{i,\beta}(s)G_d(s)Z_C(s)K_{\text{PWM}}}{Z_{L1}(s)Z_C(s) + (Z_{L2}(s) + Z_{g,\beta\beta}(s))(Z_{L1}(s) + Z_C(s) + K_{\text{PWM}}H_{ad,\beta}G_d(s))}. \tag{21}$$

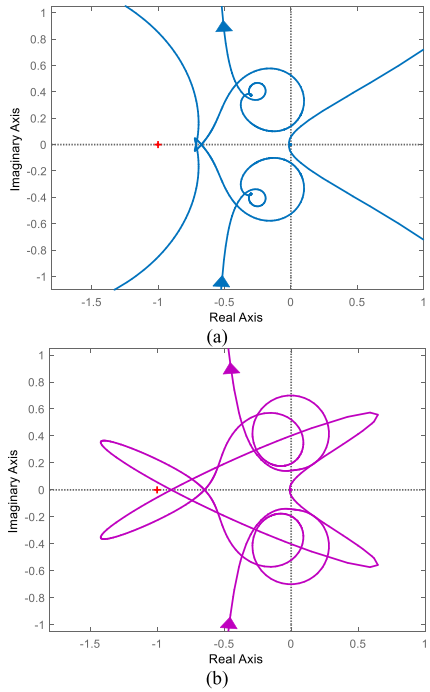

Fig. 12. Nyquist plots of the α and β loop gains with $k_{p,\alpha} = k_{p,\beta} = 13$ and $H_{ad,\alpha} = H_{ad,\beta} = 5$ (Case I) in an asymmetrical *RC* local load condition. (a) Nyquist plot of the $T_\alpha(s)$. (b) Nyquist plot of the $T_\beta(s)$.

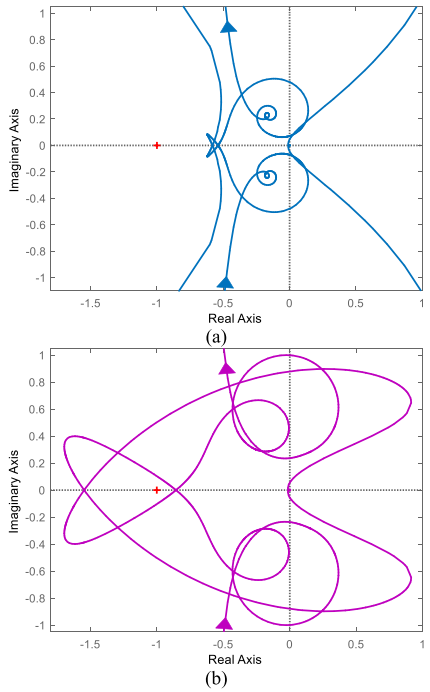

Fig. 13. Nyquist plots of the α and β loop gains with $k_{p,\alpha} = k_{p,\beta} = 10$, $H_{ad,\alpha} = 6$, and $H_{ad,\beta} = 7$ (Case II) in an asymmetrical *RC* local load condition. (a) Nyquist plot of the $T_\alpha(s)$. (b) Nyquist plot of the $T_\beta(s)$.

Fig. 12 depicts the Nyquist plots of the loop gains $T_\alpha(s)$ and $T_\beta(s)$ with the parameters that have been used in Fig. 11. This figure reveals that the subsystem in the β-axis is unstable since it encircles the critical point (–1, 0) [2], [21]. Therefore, although the α-axis is stable, the instability of the β-axis makes the whole system unstable.

The control parameters are redesigned considering the effect of system asymmetricity, and the Nyquist diagrams of loop gains $T_\alpha(s)$ and $T_\beta(s)$ are illustrated in Fig. 13, with $k_{p,\alpha} = k_{p,\beta} = 10$, $H_{ad,\alpha} = 6$, and $H_{ad,\beta} = 7$ (Case II in Table III). As shown in this figure, both subsystems are stable, which reveals that the system could work stably despite the asymmetricity of the local load. This section reveals that the stability of a grid-connected inverter could be investigated in asymmetrical grids by dividing the MIMO control system into two SISO subsystems. In this way, the stability analysis could be done easily, without neglecting the system dynamics.

V. Experimental Results

The laboratory setup shown in Fig. 14 is used to verify the validity of the proposed method for analyzing the stability of grid-connected inverters in asymmetrical grids. The hardware and control parameters are the same as those presented in Tables I–III. The control algorithm is implemented using a *dSPACE* DS1006 platform. Also, a *Chroma* 61845 is employed to mimic the utility grid

A. Asymmetricity in Grid Line Impedance

To show the accuracy of system modeling and also the validity of analysis for the case of asymmetrical grid line impedance,

Fig. 14. Experimental setup.

experiments are conducted with the same system and control parameters as presented in Section IV-A. Note that some inductors are inserted between the grid-side inductor and *Chroma* to mimic the asymmetrical grid line impedance.

Fig. 15 illustrates the experimental results of a grid-connected inverter in an asymmetrical grid line impedance condition ($L_{ga} =$ 1 mH, $L_{gb} = 4$ mH, $L_{gc} = 3$ mH), while the proportional gains of the both axes are 13 ($k_{p,\alpha} = k_{p,\beta} = 13$). This experiment is corresponding to Case I in Table II. As could be observed in Fig. 15, the injected current to the grid contains severe oscillations, which reveals that the system is unstable.

In the next experiment, just the proportional gain of the α-axis is changed to 10 ($k_{p,\alpha} = 10$), which corresponds to Case II in Table II. The experimental result for this case is presented in

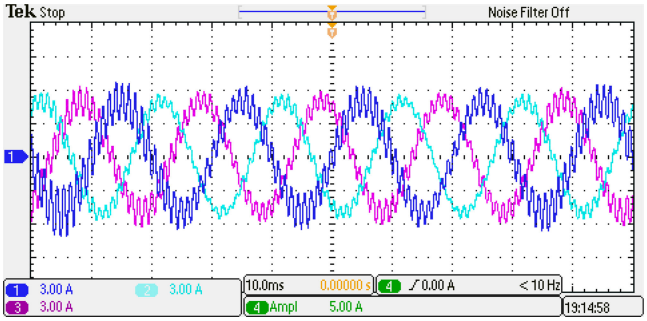

Fig. 15. Injected current to the grid in an asymmetrical grid line impedance condition with $k_{p,\alpha} = k_{p,\beta} = 13$.

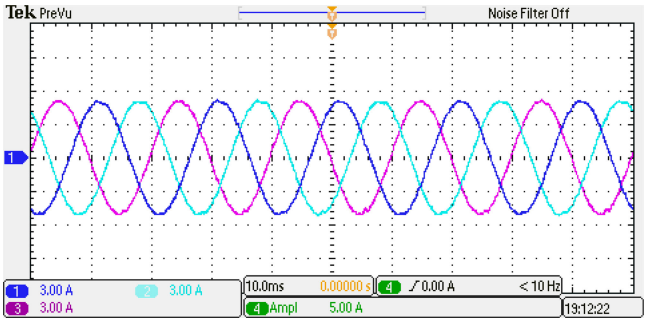

Fig. 16. Injected current to the grid in an asymmetrical grid line impedance condition with $k_{p,\alpha} = 10$ and $k_{p,\beta} = 13$.

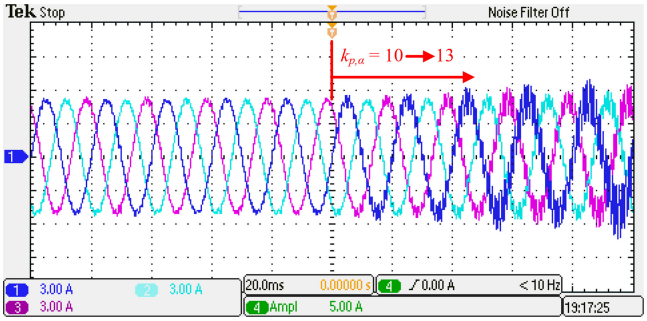

Fig. 17. Transient response of the system by changing $k_{p,\alpha}$ from 10 to 13.

Fig. 16. As could be observed, the injected current is stable, which fully validates the conclusion drawn from Fig. 8. It shows that the system is stable although the control parameters of the α- and β-axes are not identical. The results reveal that the stability analysis of an asymmetrical system could be done easily using the proposed modeling method and the system stability could be achieved by tuning the control parameters of the α and β control subsystems to ensure the stability of both axes.

Fig. 17 illustrates the transient response of the system when the proportional gain of the α-axis changes from 10 to 13. As shown in this figure, by changing $k_{p,\alpha}$ to 13, the system becomes unstable rapidly, although control parameters of the α and β subsystems are identical in this case. It indicates that neglecting the asymmetricity of the grid impedance and assuming an identical subsystem for both α- and β-axes may make the system

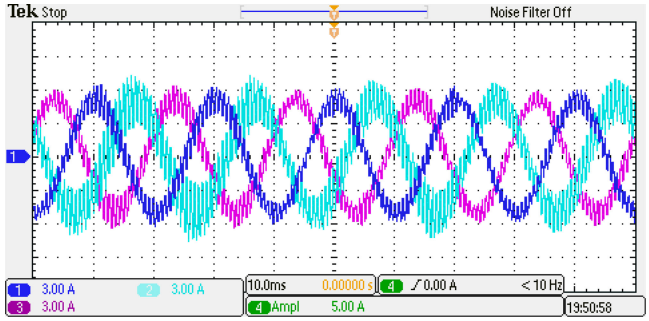

Fig. 18. Inverter output current in an asymmetrical *RC* local load condition with $k_{p,\alpha} = k_{p,\beta} = 13$ and $H_{ad,\alpha} = H_{ad,\beta} = 5$.

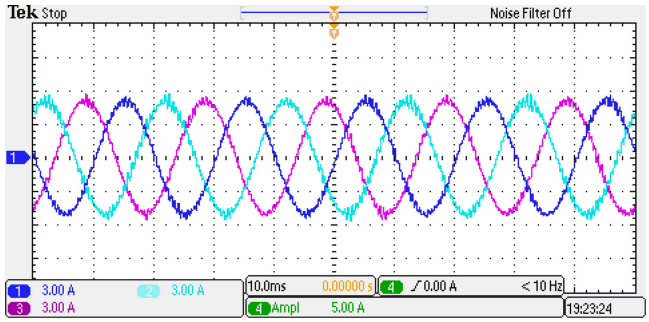

Fig. 19. Inverter output current in an asymmetrical *RC* local load condition with $k_{p,\alpha} = k_{p,\beta} = 10$, $H_{ad,\alpha} = 6$, and $H_{ad,\beta} = 7$.

unstable. Therefore, considering the asymmetricity in controller design and stability analysis steps is necessary.

B. Asymmetricity in Local Load

The experimental tests are conducted in this section to evaluate the correctness of the theoretical analysis in an asymmetrical local load condition. The control and system parameters are the same as what presented in Table III. Fig. 18 shows the experimental results for Case I in Table III (i.e., $k_{p,\alpha} = k_{p,\beta} = 13$, $H_{ad,\alpha} = H_{ad,\beta} = 5$). As could be seen in Fig. 18, the inverter output current is unstable, which is compatible with the analysis derived from Fig. 12.

The experiment is repeated using the control parameters corresponding to Case II in Table III (i.e., $k_{p,\alpha} = k_{p,\beta} = 10$, $H_{ad,\alpha} = 6$, and $H_{ad,\beta} = 7$). As shown in Fig. 19, and unlike the previous case, the system is stable, which verifies the conclusion drawn from Fig. 13. It should be noted that in this case because of capacitors in the local load, switching harmonics find a low-impedance path, and therefore, a part of switching harmonics passes through the load, instead of the filter capacitor. Hence, the waveforms in Fig. 19 contain a part of switching harmonics. However, the stability of the system is evident in comparison with Fig. 18.

The transient response of the system when the controller parameters change from Case II to Case I (in Table III) is presented in Fig. 20. As could be observed, the system becomes unstable after changing the parameters. It reveals that despite the

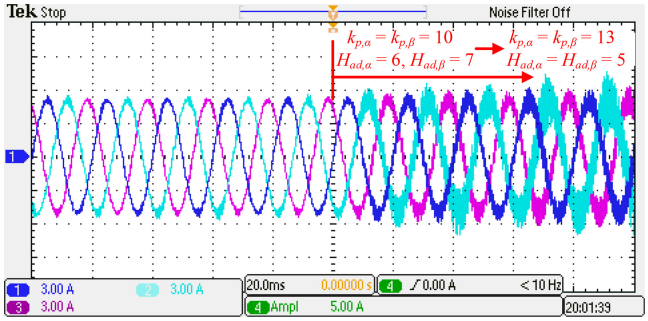

Fig. 20. Transient response of the system by changing k_p and H_{ad}.

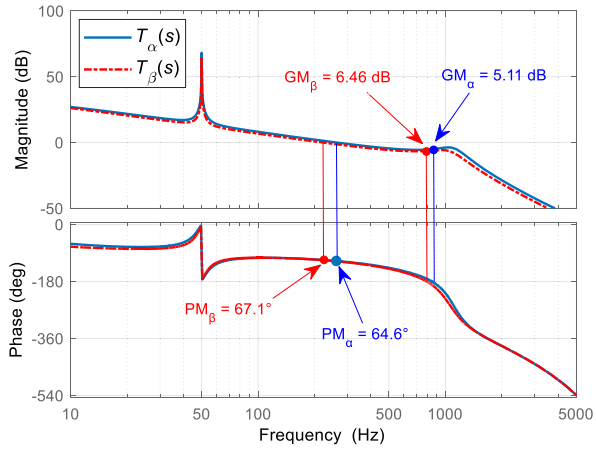

Fig. 21. Bode plots of the $T_\alpha(s)$ and $T_\beta(s)$ with $k_{p,\alpha} = 10$ and $k_{p,\beta} = 13$ (Case II in Table II) in an asymmetrical grid line impedance condition with $L_{ga} = 2$ mH, $L_{gb} = 8$ mH, $L_{gc} = 6$ mH.

stability of the α subsystem (see Fig. 12), the system is unstable because of the instability of the β subsystem.

The experimental results in this section validate the proposed method for modeling grid-connected inverters in asymmetrical grid conditions. It was shown that the asymmetricity of the system may raise instability if it is neglected in the control system design and stability analysis procedure.

C. System Robustness Against the Grid Impedance Variation

In the next experiment, the system robustness against the grid impedance variation is investigated. To this end, the control parameters in Tables I and II (Case II) which are corresponding to the stable condition when $L_{ga} = 1$ mH, $L_{gb} = 4$ mH, $L_{gc} = 3$ mH are used. To verify the system robustness, the line inductances are increased 100%, i.e., $L_{ga} = 2$ mH, $L_{gb} = 8$ mH, $L_{gc} = 6$ mH. Fig. 21 depicts the Bode diagrams of the α and β loop gains in this condition. As could be observed, both subsystems in the α- and β-axes are stable, since they have a positive PM and GM. To validate this theoretical prediction experimentally, the line inductances are suddenly increased during the experiment. Some relays have been used to bypass the new inductors (the additional inductors in comparison to the previous case) first, and then, they are opened to put those inductors in series with the previous ones, and in this way, the grid impedance increases in each line.

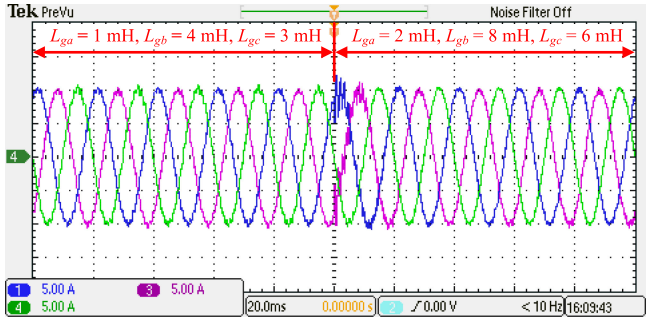

Fig. 22. Inverter output current during the grid impedance variation.

Fig. 22 shows the experimental results in this case. As could be seen in this figure, even though a severe variation is applied to the grid impedance, the system keeps its stability and injects a clean current to the grid after a very short transient.

VI. Discussion

At the end of this study, it may be helpful to briefly compare the proposed method here and the common methods in the literature for investigating the grid asymmetry effect on the converter stability. The investigations of this article are based on modeling and investigation in the linear time-invariant (LTI) framework. The result is a two-input-two-output LTI model, which is transformed into two decoupled SISO models, and investigated using SISO classic control tools. The common methods in the literature, however, are mainly based on modeling in the LTP framework, which involves some difficulties as follows.

1) The LTP modeling involves linearization around a periodic trajectory, which may be difficult.
2) The concept of the transfer function for an LTP model is elusive. This fact makes investigating LTP systems complicated. To tackle this difficulty, the concept of harmonic transfer function has been introduced, which translates the LTP system to an LTI system with infinite dimension. The infinite dimension of the HTF, however, makes its investigation impossible. To tackle this challenge, it needs to be truncated and analyzed using MIMO control tools (e.g., generalized Nyquist stability criterion), which are much more complicated than SISO tools.

Admittedly, the LTP models developed in the literature may be more accurate than the LTI one presented here. However, this increased accuracy is mostly in the low-frequency range (within the PLL bandwidth) of the converter output impedance, which is not the scope of our work.

The main advantage of the proposed method in comparison to other works is presenting a systematic and step-by-step approach for modeling the system in asymmetrical conditions. This reveals that the asymmetricity of the grid impedance may even result in negative impedance in the coupling terms [see (8)], which in turn shows the necessity of considering the effect of asymmetrical grids. On the other hand, based on Fig. 4, the effect of an asymmetrical grid still is modeled as a grid impedance (see the dashed boxes of Fig. 4). It means that the asymmetric grid

impedance effect could be investigated irrespective of the control approach that is employed for controlling the inverter. Therefore, the analysis presented in this article could be readily applied to other types of control algorithms such as inverter- and grid-current control methods, different active damping approaches, etc. Finally, dividing one MIMO system into two SISO systems makes the stability analysis easier so that classical methods could be employed for this purpose. In summary, the contributions of this article could be presented as follows:

1) developing a simple yet accurate LTI model to intuitively demonstrate the influence of the electric grid asymmetry on creating coupling between current control loops of grid-tied converters and causing instability;
2) theoretically and experimentally investigating these instabilities and identifying worst-case conditions by considering different case studies and performing different tests.

VII. Conclusion

The focus of this work lies in the stability analysis of current-controlled grid-connected inverters in asymmetrical grids. To this end, it breaks the MIMO model of the system into two SISO subsystems and in this way, the stability of the system could be analyzed using the conventional SISO methods instead of complex MIMO ones. The SISO subsystems inherit the dynamics of the MIMO system, which ensure the accuracy of the modeling. Furthermore, the inverter's control system does not affect the MIMO model derivation, which makes the modeling valid for arbitrary control systems without affecting the generality of the proposed approach. A step-by-step procedure has been presented for deriving the system model. Also, a system design guideline has been provided for tuning the control parameters in the case of asymmetrical grids. The proposed modeling method could be used for the case of asymmetricity in grid line impedance and/or local loads. The experimental results for different cases of asymmetricity verify the validity of the proposed method and theoretical analysis.

References

[1] Y. Deng, Y. Tao, G. Chen, G. Li, and X. He, "Enhanced power flow control for grid-connected droop-controlled inverters with improved stability," *IEEE Trans. Ind. Electron.*, vol. 64, no. 7, pp. 5919–5929, Jul. 2017.

[2] X. Ruan, X. Wang, D. Pan, D. Yang, W. Li, and C. Bao, *Control Techniques for LCL-Type Grid-Connected Inverters*. Singapore: Springer, 2018.

[3] Y. Han et al., "Modeling and stability analysis of *LCL*-type grid-connected inverters: A comprehensive overview," *IEEE Access*, vol. 7, pp. 114975–115001, 2019.

[4] R. Peña-Alzola, M. Liserre, F. Blaabjerg, R. Sebastián, J. Dannehl, and F. W. Fuchs, "Analysis of the passive damping losses in *LCL*-filter-based grid converters," *IEEE Trans. Power Electron.*, vol. 28, no. 6, pp. 2642–2646, Jun. 2013.

[5] D. Pan, X. Ruan, C. Bao, W. Li, and X. Wang, "Capacitor-current-feedback active damping with reduced computation delay for improving robustness of *LCL*-type grid-connected inverter," *IEEE Trans. Power Electron.*, vol. 29, no. 7, pp. 3414–3427, Jul. 2014.

[6] S. Y. Park, C. L. Chen, J. S. Lai, and S. R. Moon, "Admittance compensation in current loop control for a grid-tie *LCL* fuel cell inverter," *IEEE Trans. Power Electron.*, vol. 23, no. 4, pp. 1716–1723, Jul. 2008.

[7] Y. Jia, J. Zhao, and X. Fu, "Direct grid current control of *LCL*-filtered grid-connected inverter mitigating grid voltage disturbance," *IEEE Trans. Power Electron.*, vol. 29, no. 3, pp. 1532–1541, Mar. 2014.

[8] J. Xu, S. Xie, and T. Tang, "Active damping-based control for grid-connected *LCL*-filtered inverter with injected grid current feedback only," *IEEE Trans. Ind. Electron.*, vol. 61, no. 9, pp. 4746–4758, Sep. 2014.

[9] A. Aapro, T. Messo, T. Roinila, and T. Suntio, "Effect of active damping on output impedance of three-phase grid-connected converter," *IEEE Trans. Ind. Electron.*, vol. 64, no. 9, pp. 7532–7541, Sep. 2017.

[10] X. Wang, F. Blaabjerg, and P. C. Loh, "Virtual *RC* damping of *LCL*-filtered voltage source converters with extended selective harmonic compensation," *IEEE Trans. Power Electron.*, vol. 30, no. 9, pp. 4726–4737, Sep. 2015.

[11] Z. Xin, X. Wang, P. C. Loh, and F. Blaabjerg, "Grid-current-feedback control for *LCL*-filtered grid converters with enhanced stability," *IEEE Trans. Power Electron.*, vol. 32, no. 4, pp. 3216–3228, Apr. 2017.

[12] A. Akhavan, H. R. Mohammadi, J. C. Vasquez, and J. M. Guerrero, "Passivity-based design of plug-and-play current-controlled grid-connected inverters," *IEEE Trans. Power Electron.*, vol. 35, no. 2, pp. 2135–2150, Feb. 2020.

[13] D. Pan, X. Ruan, C. Bao, W. Li, and X. Wang, "Optimized controller design for *LCL*-type grid-connected inverter to achieve high robustness against grid-impedance variation," *IEEE Trans. Ind. Electron.*, vol. 62, no. 3, pp. 1537–1547, Mar. 2015.

[14] A. Akhavan, J. C. Vasquez, and J. M. Guerrero, "A simple method for passivity enhancement of current controlled grid-connected inverters," *IEEE Trans. Power Electron.*, vol. 35, no. 8, pp. 7735–7741, Aug. 2020.

[15] A. Akhavan, J. C. Vasquez, and J. M. Guerrero, "A robust method for controlling grid-connected inverters in weak grids," *IEEE Trans. Circuits Syst. II Exp. Briefs*, vol. 68, no. 4, pp. 1333–1337, Apr. 2021.

[16] X. Wang, F. Blaabjerg, and P. C. Loh, "Grid-current-feedback active damping for *LCL* resonance in grid-connected voltage-source converters," *IEEE Trans. Power Electron.*, vol. 31, no. 1, pp. 213–223, Jan. 2016.

[17] X. Wang, L. Harnefors, and F. Blaabjerg, "Unified impedance model of grid-connected voltage-source converters," *IEEE Trans. Power Electron.*, vol. 33, no. 2, pp. 1775–1787, Feb. 2018.

[18] H. Bai, X. Wang, P. C. Loh, and F. Blaabjerg, "Passivity enhancement of grid-tied converters by series *LC*-filtered active damper," *IEEE Trans. Ind. Electron.*, vol. 64, no. 1, pp. 369–379, Jan. 2017.

[19] J. Sun, "Impedance-based stability criterion for grid-connected inverters," *IEEE Trans. Power Electron.,* vol. 26, no. 11, pp. 3075–3078, Nov. 2011.

[20] M. Céspedes and J. Sun, "Methods for stability analysis of unbalanced three-phase systems," in *Proc. IEEE Energy Convers. Congr. Expo.*, 2012, pp. 3090–3097.

[21] W. Wu, J. Liu, Y. Li, and F. Blaabjerg, "Individual channel design-based precise analysis and design for three-phase grid-tied inverter with *LCL*-filter under unbalanced grid impedance," *IEEE Trans. Power Electron.,* vol. 35, no. 5, pp. 5381–5396, May 2020.

[22] W. Liu, X. Wang, and F. Blaabjerg, "Modeling of unbalanced three-phase grid-connected converters with decoupled transfer functions," in *Proc. IEEE Int. Power Electron. Conf.*, 2018, pp. 3164–3169.

[23] C. E. Ugalde-Loo, E. Acha, and E. Licéaga-Castro, "Analysis of the damping characteristics of two power electronics-based devices using 'individual channel analysis and design," *Appl. Math. Model.*, vol. 59, pp. 527–545, Feb. 2018.

[24] H. Zhang, L. Harnefors, X. Wang, H. Gong, and J. Hasler, "Stability analysis of grid-connected voltage-source converters using SISO modeling," *IEEE Trans. Power Electron.*, vol. 34, no. 8, pp. 8104–8117, Aug. 2019.

[25] Y. Suh and T. A. Lipo, "Control scheme in hybrid synchronous stationary frame for PWM AC/DC converter under generalized unbalanced operating conditions," *IEEE Trans. Ind. Appl.*, vol. 42, no. 3, pp. 825–835, May/Jun. 2006.

[26] W. Jin, Y. Li, G. Sun, X. Chen, and Y. Gao, "Stability analysis method for three-phase multi-functional grid-connected inverters with unbalanced local loads considering the active imbalance compensation," *IEEE Access*, vol. 6, pp. 54865–54875, 2018.

[27] J. Hu and Y. He, "Modeling and control of grid-connected voltage-sourced converters under generalized unbalanced operation conditions," *IEEE Trans. Energy Convers.*, vol. 23, no. 3, pp. 903–913, Sep. 2008.

[28] V. Salis, A. Costabeber, S. M. Cox, and P. Zanchetta, "Stability assessment of power-converter-based AC systems by LTP theory: Eigenvalue analysis and harmonic impedance estimation," *IEEE J. Emerg. Sel. Topics Power Electron.*, vol. 5, no. 4, pp. 1513–1525, Dec. 2017.

[29] P. Achlerkar and B. K. Panigrahi, "Dynamic harmonic domain modeling and stability augmented design of inverter interface to weak and unbalanced grid," *IEEE Trans. Power Del.*, to be published.

[30] C. Zhang, M. Molinas, A. Rygg, J. Lyu, and X. Cai, "Harmonic transfer-function-based impedance modeling of a three-phase VSC for asymmetric ac grid stability analysis," *IEEE Trans. Power Electron.*, vol. 34, no. 12, pp. 12552–12566, Dec. 2019.
[31] A. Doria-Cerezo, F. M. Serra, and M. Bodson, "Complex-based controller for a three-phase inverter with an *LCL* filter connected to unbalanced grids," *IEEE Trans. Power Electron.*, vol. 34, no. 4, pp. 3899–3909, Apr. 2019.
[32] Y. Liao, X. Wang, X. Yue, and L. Harnefors, "Complex-valued multi-frequency admittance model of three-phase VSCs in unbalanced grids," *IEEE J. Emerg. Sel. Topics Power Electron.*, vol. 8, no. 2, pp. 1934–1946, Jun. 2020.
[33] Q. Qian, S. Xie, J. Xu, K. Xu, S. Bian, and N. Zhong, "Output impedance modeling of single-phase grid-tied inverters with capturing the frequency-coupling effect of PLL," *IEEE Trans. Power Electron.*, vol. 35, no. 5, pp. 5479–5495, May 2020.
[34] J. Kwon, X. Wang, F. Blaabjerg, C. L. Bak, V. S. Sularea, and C. Busca, "Harmonic interaction analysis in a grid-connected converter using harmonic state-space (HSS) modeling," *IEEE Trans. Power Electron.*, vol. 32, no. 9, pp. 6823–6835, Sep. 2017.
[35] A. Akhavan, J. C. Vasquez, and J. M. Guerrero, "Stability evaluation of grid-connected microgrid clusters in asymmetrical grids," *IEEE J. Emerg. Sel. Topics Ind. Electron.*, to be published.
[36] S. Buso and P. Mattavelli, *Digital Control in Power Electronics*. San Rafael, CA, USA: Morgan & Claypool Publ., 2006.
[37] Z. Ye, W. J. Cai, and C. C. Hang, *PID Control for Multivariable Processes*. Berlin, Germany: Springer, 2008.
[38] A. Akhavan, H. R. Mohammadi, and J. M. Guerrero, "Modeling and design of a multivariable control system for multi-paralleled grid-connected inverters with *LCL* filter," *Int. J. Elect. Power Energy Syst.*, vol. 94, pp. 354–362, Jan. 2018.
[39] F. Bagheri, H. Komurcugil, O. Kukrer, N. Guler, and S. Bayhan, "Multi-input multi-output-based sliding-mode controller for single-phase quasi-Z-source inverters," *IEEE Trans. Ind. Electron.*, vol. 67, no. 8, pp. 6439–6449, Aug. 2020.
[40] A. Khaki-Sedigh and B. Moaveni, *Control Configuration Selection For Multivariable Plants*. Berlin, Germany: Springer-Verlag, 2009.
[41] K. Ogata, *Modern Control Engineering*, 4th ed. Englewood, CO, USA: Prentice-Hall, 2001.
[42] L. Harnefors, X. Wang, A. Yepes, and F. Blaabjerg, "Passivity-based stability assessment of grid-connected VSCs—An overview," *IEEE J. Emerg. Sel. Topics Power Electron.*, vol. 4, no. 1, pp. 116–125, Mar. 2016.

Ali Akhavan (Senior Member, IEEE) received the B.S., M.S., and Ph.D. degrees in electrical engineering from the University of Kashan, Kashan, Iran, in 2012, 2014, and 2019, respectively.

Since August 2019, he has been with Aalborg University, Aalborg, Denmark, where he is currently a Postdoctoral Fellow with the AAU Energy. His research interests include power electronics, modeling and control of power converters, stability analysis, and microgrid clusters.

Saeed Golestan (Senior Member, IEEE) received the B.S. degree from Shahid Chamran University of Ahvaz, Iran, in 2006, the M.S. degree from Amirkabir University of Technology, Tehran, Iran, in 2009, and the Ph.D. degree from Aalborg University, Aalborg, Denmark, in 2018, all in electrical engineering.

He is currently an Assistant Professor with the AAU Energy, Aalborg University, Aalborg, Denmark. His research interests include modeling, synchronization, and control of power electronic systems and microgrids.

Juan C. Vasquez (Senior Member, IEEE) received the B.S. degree in electronics engineering from the Autonomous University of Manizales, Manizales, Colombia, in 2004, and the Ph.D. degree in automatic control, robotics, and computer vision from BarcelonaTech-UPC, Barcelona, Spain, in 2009.

He was Assistant Professor and Associate Professor with the AAU Energy, Aalborg University, Aalborg, Denmark, in 2011 and 2014, respectively. In 2019, he became a Professor in energy internet and microgrids. He is currently the Co-Director of the Villum Center for Research on Microgrids (CROM). He was a Visiting Scholar with the Center of Power Electronics Systems (CPES), Virginia Tech, USA, and a Visiting Professor with Ritsumeikan University, Japan. He has published more than 450 journal papers in the field of microgrids, which in total are cited more than 19 000 times. His current research interests include operation, advanced hierarchical and cooperative control, optimization, and energy management applied to distributed generation in ac/dc microgrids, maritime microgrids, advanced metering infrastructures, and the integration of Internet of Things and energy Internet into the SmartGrid.

Josep M. Guerrero (Fellow, IEEE) received the B.S. degree in telecommunications engineering, the M.S. degree in electronics engineering, and the Ph.D. degree in power electronics from the Technical University of Catalonia, Barcelona, Spain, in 1997, 2000, and 2003, respectively. Since 2011, he has been a Full Professor with the AAU Energy, Aalborg University, Aalborg, Denmark, where he is responsible for the Microgrid Research Program. From 2014, he has been a Chair Professor with Shandong University; from 2015, he has been a Distinguished Guest Professor with Hunan University; and from 2016, he has been a Visiting Professor Fellow with Aston University, Birmingham, U.K.; and a Guest Professor with the Nanjing University of Posts and Telecommunications, Nanjing, China. From 2019, he has been a Villum Investigator by The Villum Fonden, Søborg, Denmark, which supports the Center for Research on Microgrids (CROM), Aalborg University, being the founder and Director of the same center. His research interests include different microgrid aspects, including power electronics, distributed energy-storage systems, hierarchical and cooperative control, energy management systems, smart metering, and the Internet of Things for ac–dc microgrid clusters and islanded minigrids. He has authored or coauthored more than 600 journal papers in the fields of microgrids and renewable energy systems, which are cited more than 50000 times. His research specially focuses on microgrid technologies applied to offshore wind, maritime microgrids for electrical ships, vessels, ferries and seaports, and space microgrids applied to nanosatellites and spacecrafts.